Journal of Instrumentation

SISSA

OPEN ACCESS

Detector and Physics Performance at a Muon Collider

To cite this article: N. Bartosik *et al* 2020 *JINST* **15** P05001

Published by IOP Publishing for Sissa Medialab

Received: *January 30, 2020*
Accepted: *March 10, 2020*
Published: *May 4, 2020*

Muon Accelerators for Particle Physics — MUON

Detector and Physics Performance at a Muon Collider

N. Bartosik,[a] **A. Bertolin,**[b] **L. Buonincontri,**[f,b] **M. Casarsa,**[c] **F. Collamati,**[d] **A. Ferrari,**[e] **A. Ferrari,**[h] **A. Gianelle,**[b] **D. Lucchesi,**[f,b,1] **N. Mokhov,**[i] **M. Palmer,**[j] **N. Pastrone,**[a] **P. Sala,**[g] **L. Sestini**[b] **and S. Striganov**[i,2]

[a] *INFN Sezione di Torino, Torino, Italy*
[b] *INFN Sezione di Padova, Padova, Italy*
[c] *INFN Sezione di Trieste, Trieste, Italy*
[d] *INFN Sezione di Roma, Roma, Italy*
[e] *CERN, Geneva, Switzerland*
[f] *University of Padova, Padova, Italy*
[g] *INFN Sezione di Milano, Milano, Italy*
[h] *HZDR, Dresden, Germany*
[i] *Fermilab, Batavia, Illinois, United States*
[j] *Brookhaven National Laboratory, Upton, New York, United States*

E-mail: donatella.lucchesi@pd.infn.it

Abstract: A muon collider represents the ideal machine to reach very high center-of-mass energies and luminosities by colliding elementary particles. This is the result of the low level of beamstrahlung and synchrotron radiation compared to linear or circular electron-positron colliders. In contrast with other lepton machines, the design of a detector for a multi-TeV muon collider requires detailed knowledge of the interaction region due to the significant backgrounds created by muon beam decays in the collider ring. The physics reach can be properly evaluated only when the detector performance in such an environment is determined. In this work, the backgrounds generated by muon beams of 750 GeV are characterized and the performance of the tracking system and the calorimeter detector is illustrated. Solutions to minimize the effect of the beam-induced backgrounds are discussed and applied to obtain track and jet reconstruction performance. The $\mu^+\mu^- \to H\nu\bar{\nu} \to b\bar{b}\nu\bar{\nu}$ process is fully simulated and reconstructed to demonstrate that physics measurements are possible in this harsh environment. The measurement precision for the Higgs boson coupling to $b\bar{b}$ is evaluated for $\sqrt{s}$ = 1.5, 3, and 10 TeV and compared to other proposed machines.

Keywords: Detector modelling and simulations I (interaction of radiation with matter, interaction of photons with matter, interaction of hadrons with matter, etc); Performance of High Energy Physics Detectors; Large detector systems for particle and astroparticle physics

ArXiv ePrint: 2001.04431

[1] Corresponding author.
[2] Deceased.

https://doi.org/10.1088/1748-0221/15/05/P05001

Contents

2020 JINST 15 P05001

1 Introduction

In a multi-TeV muon collider, the effects of backgrounds created by decays from the muon beam in the collider ring must be evaluated in detail at the detector level in order to estimate the physics reach. Muon decay products can contaminate the Interaction Region (IR) from a distance that varies with the beam energy. Thus, the design of the collider optics, including superconducting magnets with appropriate protective elements, must be included in the detector simulations [1] to have an accurate background description. Previous studies [2–4] have found that two cone-shaped tungsten shields can be used to protect the IR and the detector from the extremely high flux of beam background particles. As a consequence, the exact design of the machine-detector interface (MDI), which includes these shields, is needed to evaluate the distribution of the induced background at any part of the detector.

Beam-induced backgrounds generated by the MAP collaboration [5], using an IR and MDI optimized for 1.5-TeV center-of-mass energy [3], are used to study the effect on the performance of the tracking system and calorimeter detector. The software framework used for the propagation of the beam-induced background through the detector is inherited from the MAP collaboration and has been further developed to obtain the final results. The production and decay of the Higgs boson $\mu^+\mu^- \to H\nu\bar{\nu} \to b\bar{b}\nu\bar{\nu}$ at $\sqrt{s} = 1.5$ TeV are studied to determine the reconstruction and identification efficiencies, which are then used to evaluate the sensitivity to the $b\bar{b}$ coupling.

Samples of $\mu^+\mu^- \to H\nu\bar{\nu} \to b\bar{b}\nu\bar{\nu}$ at particle-level have also been generated at $\sqrt{s} = 3, 10$ TeV and a conservative estimate of the sensitivities at these energies is presented.

2 Beam-induced background characterization

The simulation of beam-induced backgrounds has been performed with the MARS15 software [6] and studied for machines with a center-of-mass energy of $\sqrt{s} = 1.5$ TeV and $\sqrt{s} = 125$ GeV, as discussed in detail in refs. [3, 4] and in ref. [7]. The background particles reaching the detector are mainly produced by the interactions of the decay products of the muon beams with the machine elements. Their type, flux, and characteristics strongly depend on the machine lattice and the interaction point configuration, which in turn depend on the collision energy. The background particles reaching the detector region may be produced tens of meters upstream of the interaction point, as can be seen in figure 1. Therefore, a detailed layout of the machine and the machine-detector interface must be included in the simulation. In particular, the opening angle of two shielding cones ("nozzles"), which are introduced to mitigate the effects of the beam-induced backgrounds inside the detector, must be optimized for a specific beam energy and will affect the detector acceptance. At present, the nozzles have only been optimized for a 1.5 TeV center-of-mass energy.

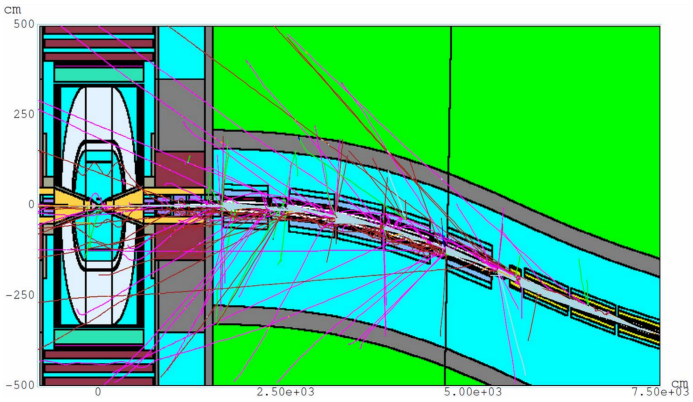

Figure 1. Illustration of the model of the machine and machine-detector interface used in the MARS15 simulation. The shielding nozzles, described in the text, are represented in yellow inside the detector. This figure has been reproduced from ref. [8].

Even with an optimized IR design, the flux of particles penetrating the shielding and reaching the detector volume is quite high. The main properties of these particles are a relatively low momentum and an arrival time in each sub-detector asynchronous with respect to the beam crossing. Figure 2 shows the momentum spectra of the electromagnetic (left) and hadronic (central) components of the beam-induced backgrounds for a muon beam of 750 GeV by assuming $2 \cdot 10^{12}$ muons per bunch and a luminosity $\mathcal{L} = 1.25 \cdot 10^{34}\,\mathrm{cm}^{-2}\mathrm{s}^{-1}$. The former is relatively soft ($\langle p_{\mathrm{ph.}} \rangle = 1.7$ MeV and $\langle p_{\mathrm{el.}} \rangle = 6.4$ MeV), whereas the latter has an average momentum of about half a GeV ($\langle p_{\mathrm{n}} \rangle = 477$ MeV and $\langle p_{\mathrm{ch.had.}} \rangle = 481$ MeV). The time of arrival of the particles at the detector entry point with respect to the bunch crossing time for the different background components is shown on the right of figure 2. The peaks that are evident around zero are primarily due to the leakage of photons and electrons around the interaction point, where the shielding is minimal.

2020 JINST 15 P05001

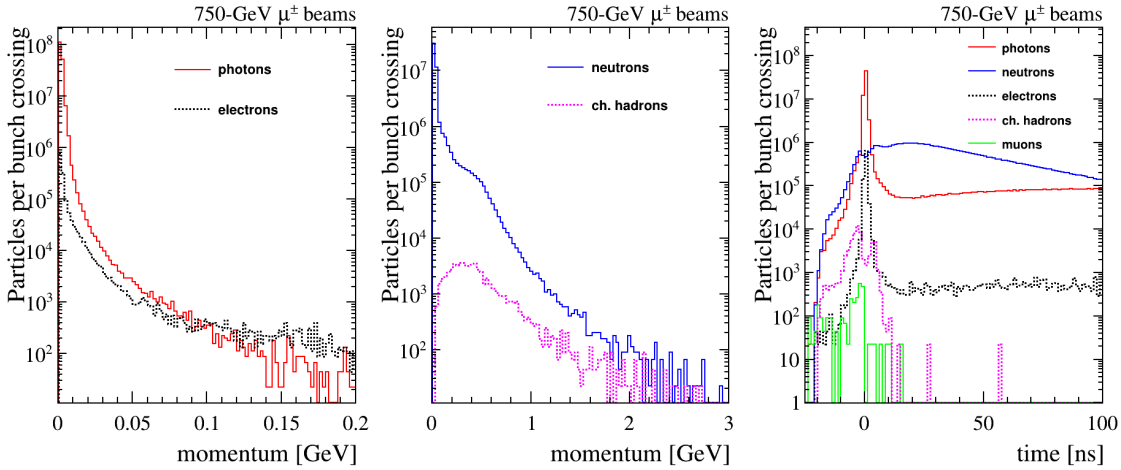

Figure 2. Characteristics of the beam-induced background particles at the detector entry point: the momentum spectra for photons and electrons and for neutrons and charged hadrons are shown in the left and central panels, respectively; the time of arrival with respect to the beam crossing time is shown on the right.

3 Detector performance

The detector model and software framework used for the studies presented in this paper can also be found in ref. [7, 8]. Figure 3 presents a schematic view of the detector components, as implemented in the ILCRoot framework [9]. These studies focus on the tracking and calorimeter systems, a full simulation of the muon detector is not currently available. Both the tracker and the calorimeter are immersed in a solenoidal magnetic field of 3.57 T.

The tracking system consists of a vertex detector (VTD), an outer silicon tracker (SiT) and a forward tracker (FTD). The vertex detector, located just outside a 400-μm thick Beryllium beam pipe of 2.2-cm radius, is 42-cm long with five cylindrical layers at distances from 3 to 12.9 cm in the transverse plane to the beam axis and four disks on each end. Outside the VTD, a 330-cm long silicon tracker is comprised of five cylindrical layers at radial distances between 25 and 126 cm and 7 + 7 forward disks.

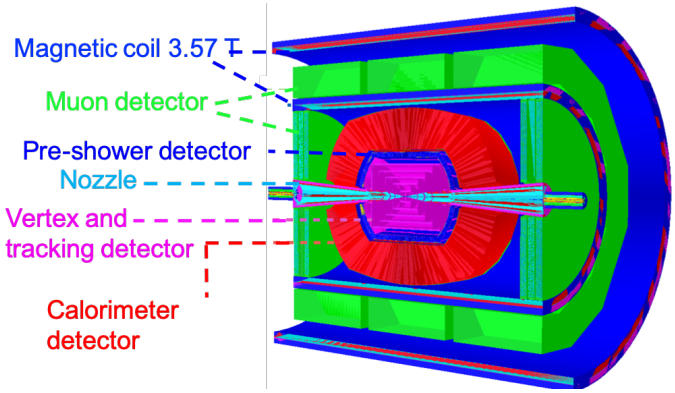

Figure 3. Schematic view of the detector, with each component identified by the label.

2020 JINST 15 P05001

The forward tracker consists of three disks on each side of the SiT at $z = \pm 120, \pm 155, \pm 190$ cm, which cover the very forward regions and are properly shaped to accommodate the nozzles. The silicon sensors of all the tracking detectors are based on silicon pixel technology. The VTD sensors have a pixel granularity of $20 \times 20\,\mu m^2$ and a thickness of 75 µm in the barrel and 100 µm in the disks. The SiT and the FTD feature pixel sensors of 50×50-μm^2 pitch and 200-µm thickness. The full simulation output is digitized, with signals that include electronic noise as well as threshold and saturation effects.

Despite the mitigation of the beam-induced backgrounds provided by the shielding nozzles, a large particle flux reaches the detector, causing a very high occupancy in the first layers of the tracking system that impacts the detector performance. Next-generation 4D silicon sensors [10], which provide both spatial and time information, would allow exploitation of the broad time distribution of the background hits and remove a significant fraction of them. An optimized hit selection time window for each tracking layer was studied in a sample of muons, generated at the IP with a flat p_T spectrum between 0.5 and 100 GeV. The distributions of the arrival times registered by

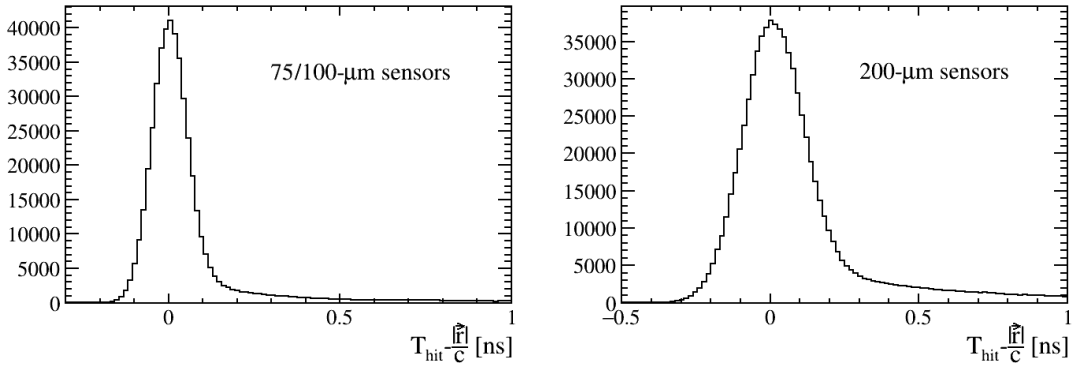

Figure 4. Distributions of the tracker hit times with respect to the bunch crossing for 75 µm/100 µm-thick sensors (left) and 200 µm-thick sensors (right) in a sample of muons with $0.5 < p_T < 100$ GeV. The tails on the right are due to the low-momentum muons.

each sensor with respect to the bunch crossing are shown in figure 4, where average time resolutions σ_T of 50 ps and 100 ps are assumed for the sensors with a thickness of 75 µm/100 µm and 200 µm, respectively [11]. The contribution to the time resolution due to the time spread of the beam spot is estimated to be $\sim$ 30 ps. Figure 5 shows the reduction in occupancy of the tracker layers when the hit times are required to be consistent with the arrival time of particles produced at the IP within a $\pm 3\,\sigma_T$ window.

The calorimeter response is fully simulated for a Dual-Readout Integrally Active and Non segmented Option (ADRIANO) [12]. The geometry is fully projective, covering polar angles down to 8.4°. Barrel and end-cap regions are formed by approximately 23600 towers of 1.4° aperture angle of lead glass with scintillating fibers. Cherenkov and scintillation hits are generated separately and digitized independently. The full simulation includes the effects of photodetector noise, wavelength-dependent light attenuation, collection efficiency and energy cluster digitization. Beam-induced backgrounds generate an almost flat distribution of noise in each tower, similar to an underlying event as displayed on the left panel of figure 6. Part of this noise is removed by the jet

2020 JINST 15 P05001

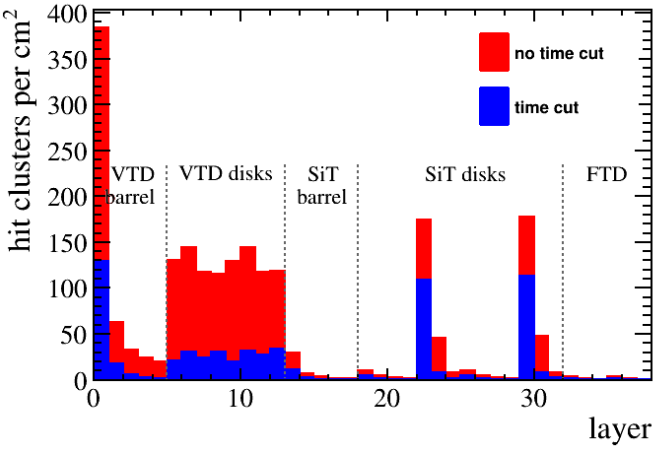

Figure 5. Hit density for each tracker layer before and after applying the time requirements.

clustering algorithm as discussed in 3.2. The study of energy deposition from prompt muon events demonstrates that the calorimeter response, as currently implemented, is isotropic. Therefore the visible features in the angular distribution in figure 6 are produced by the beam-induced backgrounds.

The time of the energy deposit in each calorimeter tower can be further exploited to suppress the beam-induced backgrounds. In the right panel of figure 6, the arrival time distribution (in black) for all energy clusters is compared to the primary muon arrival time distribution (in red). The late component can be removed by applying a proper time window, which must be optimized tower by tower. However this timing information is not used in the present studies and, thus, better results are expected in the future.

The energy deposited by the beam-induced backgrounds on each bunch crossing as a function of calorimeter depth is shown in figure 7. With the current detector design, the beam-induced background particles are not fully contained, but the released energy is reduced by roughly a factor 20 from the first to the last calorimeter layers. The residual energy flux, about 500 keV/cm^2, can be easily reduced by an absorber in front of the muon detector. For example, the reduction in flux due to the presence of the magnet coil in this design is not yet included in the present simulation.

3.1 Track reconstruction performance

Hits surviving the selection criteria discussed in section 3 are used as an input to a parallel Kalman filter, as implemented in the ILCRoot framework. Pattern recognition and track finding are performed simultaneously using an iterative procedure with increasing search windows for hits in the following tracker layers at each iteration. This method guarantees high tracking efficiency, but requires significant computing resources and long processing times. With the available code, only four iterations were feasible for events including beam-induced backgrounds. Figure 8 shows the tracking efficiency evaluated in a sample of muons as a function of transverse momentum (p_T) and pseudorapidity (η) for different numbers of iterations. The tracking efficiency is defined as the fraction of generated particles in the tracker geometrical acceptance that are matched to a good-quality reconstructed track. The effect of fewer iterations in the track finding procedure is a drop in efficiency for low-p_T and high-η particles. Four iterations represented a good trade-off between

2020 JINST 15 P05001

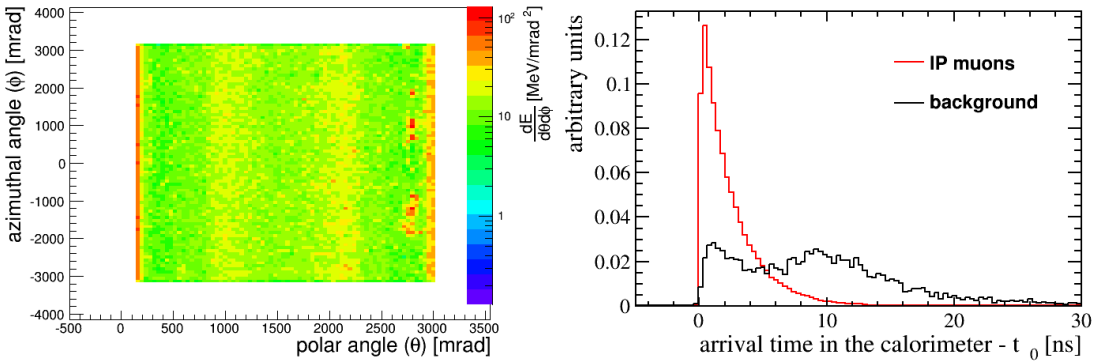

Figure 6. Left: energy distribution in the calorimeter of the beam-induced backgrounds. Right: distribution of the arrival time at a given calorimeter position of particles generated by beam radiation and of muons coming from primary vertex. The particles arrival time is measured with respect to t_0, defined as the arrival time in the given position of a photon produced in the primary vertex at the collision time

.

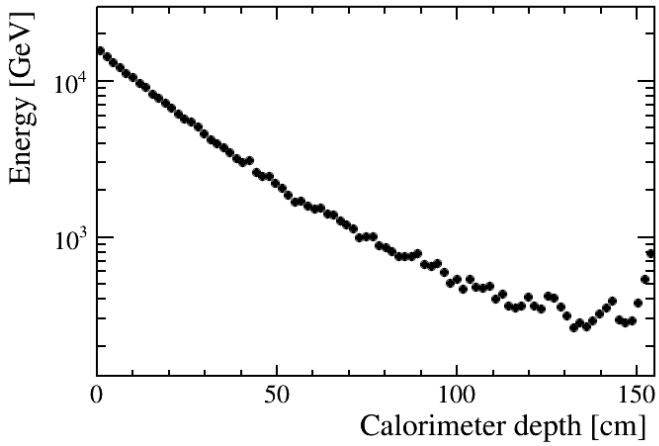

Figure 7. The energy deposited in the calorimeter by beam-induced backgrounds on each bunch crossing as a function of the calorimeter depth.

reconstruction efficiency and processing time. As an example, the tracking of one beam-induced background event, $\sim$ 60000 tracks with $p_T > 0.5$ GeV, through 4 iterations takes approximately one hour on an Intel Xeon CPU E5-2665 2.40GHz with 32GB RAM. The CPU time increases non-linearly with the number of iterations.

The track reconstruction performance is assessed in samples of single muons generated with different momenta and pseudorapidities. The left panel of figure 9 shows the tracking efficiency as a function of transverse momentum for three representative values of $|\eta|$: the tracker central region, the forward region, and the crack between the two. As expected, there is a loss of efficiency at low transverse momentum, which can be seen more clearly on the right panel, where the efficiency is plotted as a function of $|\eta|$ for three different generated momentum values. Low efficiency at high $|\eta|$ is expected both due to the lower performance of the reconstruction algorithm and the limited coverage of the detector with the shielding nozzles. The relative transverse momentum resolution

2020 JINST 15 P05001

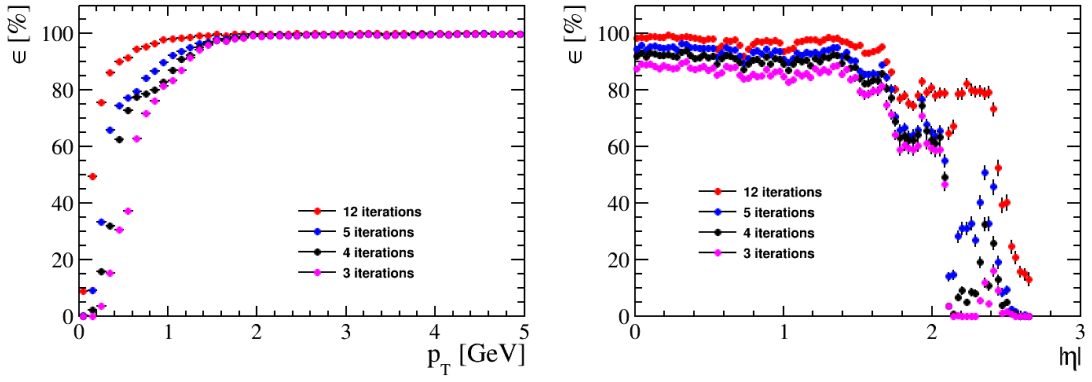

Figure 8. Tracking efficiency for different numbers of iterations as a function of the transverse momentum p_{T} (left) and the psudorapidity $|\eta|$ (right) in a sample of muons.

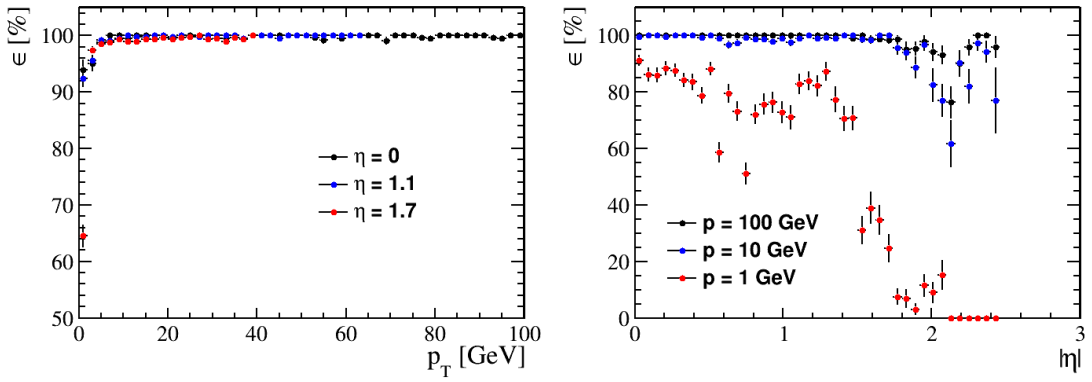

Figure 9. Muon tracking efficiency as a function of p_{T} for three representative $|\eta|$ values (left) and as a function of $|\eta|$ for three different generated momenta (right).

of the reconstructed tracks is reported in figure 10 for samples of single muons. The left panel shows the track p_{T} resolution as a function of p_{T} in different $|\eta|$ regions. In the central and forward regions the p_{T} resolution is less than 5×10^{-4} GeV^{-1} for $p_{\mathrm{T}} > 10$ GeV, while tracks reconstructed in the crack between the central layers and the forward disks present a degraded resolution. The right panel shows the p_{T} resolution as a function of pseudorapidity for muons with generated p = 1, 10, 100 GeV. The resolution degrades visibly for tracks of low transverse momentum and high $|\eta|$.

3.2 Jet reconstruction and identification performance

Jet reconstruction was not part of the ILCRoot package and a simple dedicated algorithm that takes into account the high yield of particles coming from the beam-induced background has been developed. Jet reconstruction is performed using the calorimeter clusters, which are selected according to the following algorithm:

1. the calorimeter detector is divided into several pseudorapidity regions of equal width;
2. in each region the mean $\langle E \rangle$ and the standard deviation σ_E of the calorimeter cluster energies are calculated;

2020 JINST 15 P05001

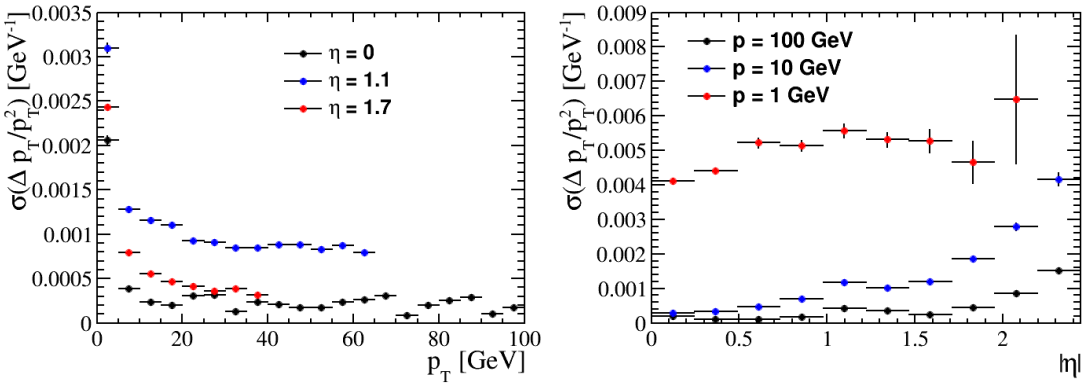

Figure 10. Track p_T resolution as a function of p_T (left) for three representative values of $|\eta|$ and as a function of $|\eta|$ (right) for three generated ranges of muon momenta. Each bin has been calculated as the width of the distribution $\Delta p_T/p_T^2$, where Δp_T is the difference between the true muon p_T and the p_T of the corresponding reconstructed track.

3. calorimeter clusters with an energy E higher than $\langle E \rangle + 2 \cdot \sigma_E$ are selected;

4. the energy of the selected clusters is corrected by subtracting the mean value $\langle E \rangle$ of the corresponding region.

This selection algorithm is designed to remove, at least in part, the beam-induced background that is diffused in the calorimeter as shown in figure 6. In this way, signals originated by particles coming from the primary interaction, are identified as energy deposition significantly above the mean background energy.

Selected calorimeter clusters are then used as inputs to the jet clustering algorithm: a cone algorithm [13] with a radius parameter of $R = 0.5$ is employed, where R is defined as $R = \sqrt{\Delta\eta^2 + \Delta\phi^2}$ with $\Delta\eta$ ($\Delta\phi$) the difference between η (ϕ) of the jet axis and the one of each cluster. Calorimeter clusters with an energy greater than 2 GeV are considered as seeds. The raw jet energy is obtained as the sum of the energies of the clusters belonging to the jet.

In order to evaluate the jet energy corrections needed to assess the jet algorithm performance, a simulated sample of $\mu^+\mu^- \rightarrow H(\rightarrow b\bar{b})\nu\bar{\nu}$ events at $\sqrt{s} = 1.5$ TeV is used. This physics process has been generated at particle level with Pythia 8 [14] and the full simulation with beam-induced backgrounds is employed to obtain the detector response. Truth-level jets are clustered by using truth-level stable particles as inputs to the cone algorithm. Then a reconstructed, detector-level jet is matched with a truth-level jet if the distance in the (η, ϕ) space between their axes is less than 0.5. Reconstructed jets that fulfill this requirement are designated as truth-matched jets.

The average truth-level jet transverse momentum (p_T) is shown in figure 11 as a function of the jet raw p_T. It is evident that the truth-level jet p_T is strongly correlated with the raw jet p_T demonstrating the correctness of the reconstruction. A polynomial fit to the graph is performed in order to obtain the jet energy correction function, which is applied to the reconstructed-level jets to determine the nominal jet energy starting from the raw jet energy.

The jet transverse momentum resolution $\frac{\Delta p_T}{p_T}$ is defined as the difference between the jet p_T and the matched truth-level jet p_T, divided by the truth-level jet p_T. The average $\frac{\Delta p_T}{p_T}$ as a function of

2020 JINST 15 P05001

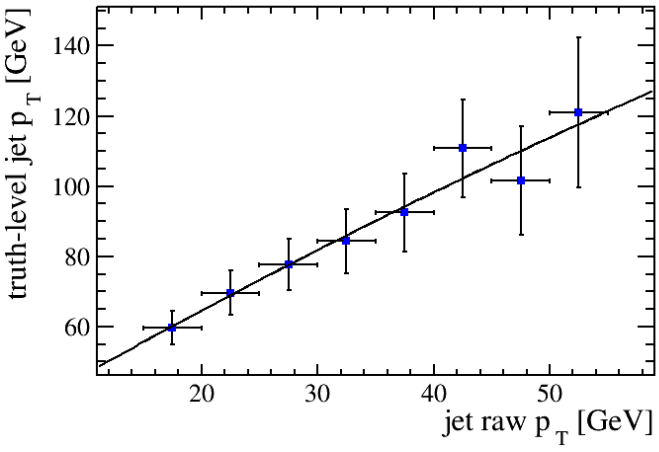

Figure 11. Truth-level jet p_{T} as a function of the raw p_{T} of reconstructed jets.

the jet transverse momentum is shown in figure 12 (left) for simulated b-jets. The resolution varies from 30% to 40% depending on the jet p_{T}.

The jet reconstruction efficiency, the number of reconstructed jets matched with truth-level jets divided by the total number of truth-level jets is shown, as a function of the jet transverse momentum, on the right of figure 12. The efficiency is around 50% for low-p_{T} jets and around 70% for $p_{\mathrm{T}} > 60$ GeV.

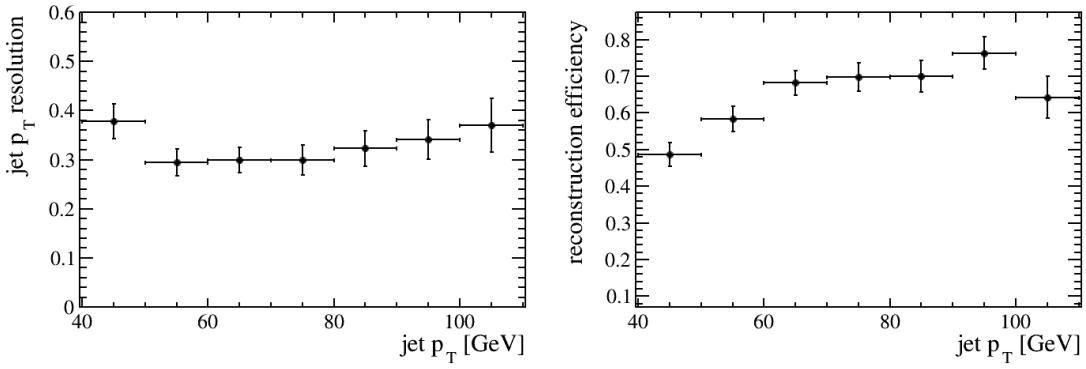

Figure 12. Left: average jet transverse momentum resolution as a function of the jet transverse momentum. Right: jet reconstruction efficiency as a function of the jet transverse momentum.

The rate of fake jets is not really meaningful: the algorithm is not optimized and a better jet reconstruction method will be available in the future by implementing a Particle Flow algorithm that considers both tracks and calorimeter clusters as inputs. In order to give an idea of the performance on the current reconstruction, the number of reconstructed jets not matched with a truth-level jet divided by the total number of reconstructed jets is evaluated. The fake-rate is found to be of the order of 25% for jets with $p_{\mathrm{T}} > 40$ GeV.

2020 JINST 15 P05001

4 Reconstruction of Higgs boson decay to b-jets

The $H \to b\bar{b}$ final state is identified in two steps: the identification of b-jets and the selection of the $b\bar{b}$ resonance among physics background events.

4.1 b-jet identification algorithm and performance

A b-jet tagging algorithm has been developed to reduce the background coming from light quark and gluon jets and from fake jets originated by several background sources in particular the beam-induced background. The algorithm is inspired by the one employed by the LHCb collaboration [15] and uses tracks inside the jet cone to identify decay vertices compatible with b-hadron decays. The algorithm has the following steps:

1. For a given reconstructed jet, tracks inside the jet cone are selected, requiring that each track has p_{T} greater than 500 MeV and an impact parameter with respect to the $\mu^+\mu^-$ interaction point greater than 0.04 cm. Only good quality tracks are selected by requiring a minimum number of hits;

2. 2-track vertices are formed by requiring the distance of closest approach between the tracks to be less than 0.02 cm. The total p_{T} of the two tracks must be greater than 2 GeV;

3. 3-track vertices are formed by linking two 2-track vertices that share one track;

4. If at least one 3-track vertex is found, then the jet is tagged as a b-jet.

This algorithm is very simple and cut-based. Higher performance methods that exploit machine learning techniques are currently available. In the future the most suitable algorithm, tuned for the process under study, will be applied.

The limitations on track reconstruction, as explained in section 3.1, prevent application of the b-jet tagging algorithm to the full event, $\mu^+\mu^- \to H(\to b\bar{b})\nu\bar{\nu}$ with the beam-induced backgrounds overlay. Thus the overall performance is evaluated separately and then applied to the Higgs boson reconstruction. In figure 13 the two most discriminating observables associated with a secondary vertex (SV) in truth-matched b-jets are compared with SVs found in background events, in this particular case the beam-induced background. The two observables are the invariant mass of the tracks belonging to the SV and the pseudo-lifetime, defined as $\tilde{t} = \frac{m_{B^0} \cdot d}{p}$, where m_{B^0} is the nominal B^0 mass, d is the secondary vertex distance from the interaction point and p is the overall momentum of the tracks associated with the SV. It is evident that any reasonable algorithm should have the performance to efficiently select b-jets.

The b-tagging efficiency is defined as the number of tagged and reconstructed b-jets divided by the total number of reconstructed b-jets. The b-tagging efficiency as a function of the jet p_{T} is presented in figure 14. It can be seen that it varies from about 40% at low jet p_{T} to about 60% at high jet p_{T}. These values are very close to what is currently obtained in analyses of the LHC experiments. The mis-identification rate is evaluated on a statistical basis since it is not possible to determine it directly by using beam-induced background events due to tracking limitations. The (η, ϕ) space is divided in cone regions with $R = 0.5$, in each cone SVs are reconstructed with the b-tagging algorithm. The ratio between the number of cones with at least one fake SV and the total

2020 JINST 15 P05001

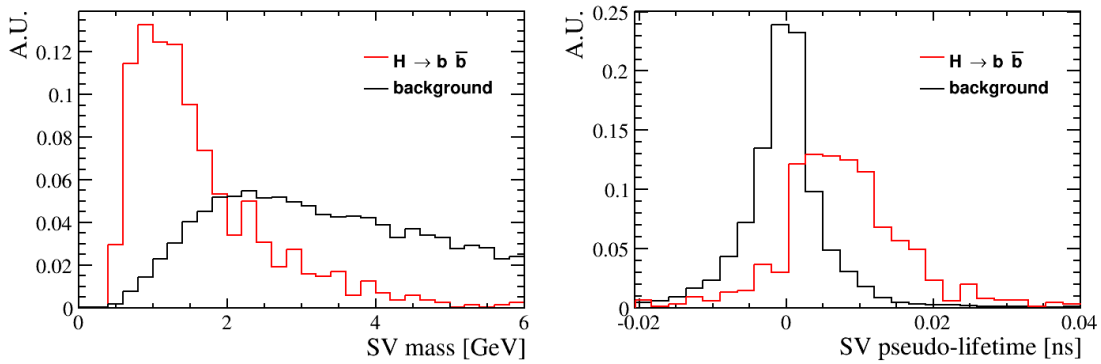

Figure 13. Left: invariant mass of tracks associated with a SV for truth-matched b-jets from Higgs decay events (red) and for beam-induced background events (green). Right: pseudo-lifetime for truth-matched b-jets from Higgs decay events (red) and for beam-induced backgrounds (green). A negative pseudo-lifetime is assigned if the d projection with respect to the jet axis is negative.

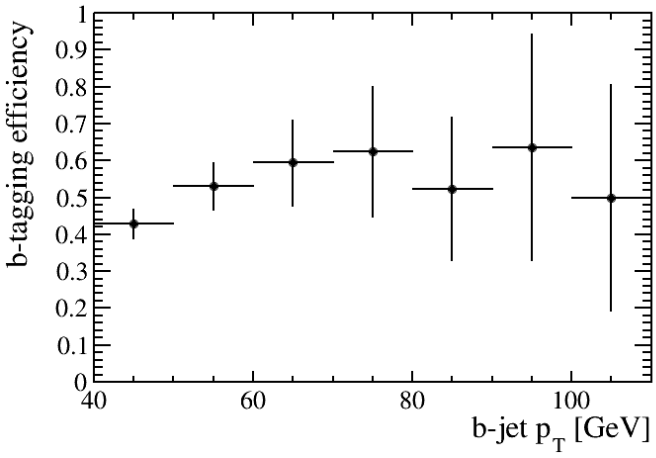

Figure 14. b-tagging efficiency as a function of the jet p_{T}.

number of cones is taken as the misidentification rate. It varies between 1% and 3% depending on the requirements on the tracks. In this way the effect of the beam induced background on the Higgs boson identification is included through the b-tagging efficiency.

4.2 $H \to b\bar{b}$ selection

The $\mu^+\mu^- \to H(\to b\bar{b})\nu\bar{\nu}$ events generated at $\sqrt{s} = 1.5$ TeV are reconstructed by a simple procedure. The fiducial region is defined by two jets with $p_{\mathrm{T}} > 40$ GeV and pseudorapidity in the range $-2.5 < \eta < 2.5$. Therefore, the first requirement is to have two reconstructed and b-tagged jets in the fiducial region. The acceptance, A, is defined as the number of events with two b-jets from Higgs boson decay in the fiducial region divided by the number of generated $H \to b\bar{b}$ events. At $\sqrt{s} = 1.5$ TeV the acceptance is found to be $A = 0.35$. The selection efficiency (ϵ) is defined as the number of fully reconstructed $H \to b\bar{b}$ events divided by the number of events with two truth-level b-jets from Higgs boson decay in the fiducial region, and it is found to be $\epsilon = 15\%$. The reconstructed di-jet invariant

2020 JINST 15 P05001

mass of truth-matched b-jets in $H \to b\bar{b}$ events is shown in figure 15. The presence of the beam-induced background could have jeopardized this distribution making the Higgs boson identification very difficult. Instead the Higgs boson peak is clearly visible in the di-jet invariant mass.

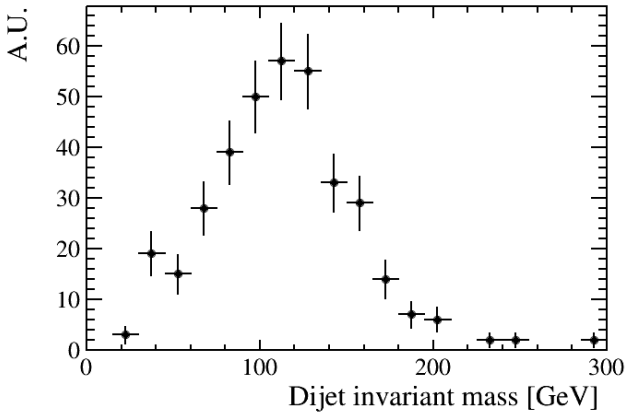

Figure 15. The di-jet invariant mass of truth-matched b-jets in $H \to b\bar{b}$ full-simulated events at $\sqrt{s} = 1.5$ TeV.

5 Higgs Boson coupling to b-quark

In addition to demonstrating that one of the most critical decay channels, $H \to b\bar{b}$, is reconstructed efficiently at a muon collider, the achievable sensitivity on the couplings is evaluated for three different center-of-mass energies.

5.1 Higgs Boson coupling to b-quark at $\sqrt{s} = 1.5$ TeV

In this section the sensitivity of the measurement of the Higgs boson coupling to b quarks (g_{Hbb}) in $\mu\mu$ collisions at $\sqrt{s} = 1.5$ TeV is studied. Since the Higgs boson production at $\sqrt{s} = 1.5$ TeV is dominated by WW fusion [7] the $H \to b\bar{b}$ production cross section (σ) is related to the Higgs boson couplings as follows:

$$\sigma = \sigma(\nu\nu H) \cdot BR(H \to b\bar{b}) = \frac{g^2_{HWW} g^2_{Hbb}}{\Gamma_H}, \tag{5.1}$$

where g_{HWW} is the coupling of the Higgs boson to the W boson and Γ_H is the Higgs boson width. The uncertainty on g^2_{Hbb} is, therefore, related to the measured cross section.

The number of observed $H \to b\bar{b}$ events (N) is given by:

$$N = A \cdot \epsilon \cdot \sigma \cdot \mathcal{L} \cdot t, \tag{5.2}$$

where A is the acceptance, ϵ is the selection efficiency, $\mathcal{L}$ is the instantaneous luminosity and t is the data-taking time. By using a sample of events generated with Pythia 8, which are fully simulated and reconstructed following the procedure described above, the $H \to b\bar{b}$ cross section at $\sqrt{s} = 1.5$ TeV is found to be $\sigma = 203$ fb. Therefore, with an instantaneous luminosity of $\mathcal{L} = 1.25 \cdot 10^{34}\,\mathrm{cm}^{-2}\mathrm{s}^{-1}$ in a data taking period of four Snowmass years ($t = 4 \cdot 10^7$ s) the number of observed Higgs boson events decaying to $b\bar{b}$ is $N = 5500$.

2020 JINST 15 P05001

The uncertainty on the cross section determination is calculated by assuming that A, ϵ, $\mathcal{L}$, and t are known with a good precision, and it is given, approximately, by the number of events after all the selection criteria are applied:

$$\frac{\Delta\sigma}{\sigma} \simeq \frac{\sqrt{N+B}}{N}, \tag{5.3}$$

where B is the expected number of background events. In principle, with a combined fit to the di-jet invariant mass and discriminating kinematic variables, it should be possible to disentangle the signal from the background, thus reducing the uncertainty on the cross section. In this study, a conservative estimate based on equation (5.3) is used to evaluate the uncertainty on the cross section.

The contribution to the background events comes from two sources: physics processes and uncorrelated background. The first contribution is evaluated with Monte Carlo simulation. The Standard Model processes considered as possible background are listed in table 1. The number of

Table 1. List of Standard Model processes considered in the background estimation for the $H \to b\bar{b}$ cross section measurement. q indicates a generic quark.

Process
$\mu^+\mu^- \to \gamma^*/Z \to q\bar{q}$
$\mu^+\mu^- \to \gamma^*/Z\gamma^*/Z \to q\bar{q} + \mathrm{X}$
$\mu^+\mu^- \to \gamma^*/Z\gamma \to q\bar{q}\gamma$

background events with $b\bar{b}$ final states has been estimated by applying reconstruction and b-tagging efficiencies to generator-level samples produced with Pythia 8. The contribution of light quark events, for example those with two b-tags in the final state that are due mainly to beam-induced background, has been calculated by applying the same procedure as used for the physics processes. In this case, however, the tagging mis-identification rate is used instead of the b-tagging efficiency. The fake-jet contribution, after the b-tagging requirements, is negligible. The number of expected background events after considering all the contributions, is $B = 6700$. At this point it is possible to evaluate the uncertainty on the cross section by using equation (5.3), $\frac{\Delta\sigma}{\sigma} = 2.0\%$.

According to equation (5.1), it is necessary to also know g_{HWW} and Γ_H in order to determine g_{Hbb}. Knowledge of the $H \to b\bar{b}$ cross section is not enough. In the following, it is assumed that g_{HWW} and Γ_H can be measured with the same level of precision expected by CLIC at $\sqrt{s} = 1.4$ TeV [16]. This is justified by the fact that the selection of muonic final states at a muon collider is analogous to that at electron-positron accelerators, since the beam-induced background stops at the calorimeters and is not expected in muon detectors. Therefore the uncertainty on the coupling can be obtained with:

$$\frac{\Delta g_{Hbb}}{g_{Hbb}} = \frac{1}{2}\sqrt{\left(\frac{\Delta\sigma}{\sigma}\right)^2 + \left(\frac{\Delta\frac{g^2_{HWW}}{\Gamma_H}}{\frac{g^2_{HWW}}{\Gamma_H}}\right)^2}, \tag{5.4}$$

where the uncertainty on $\frac{g^2_{HWW}}{\Gamma_H}$ has been extracted from the CLIC study [16] and scaled for the lower integrated luminosity assumed for the muon collider at $\sqrt{s} = 1.5$ TeV. The expected sensitivity on the Higgs coupling to b quark at $\sqrt{s} = 1.5$ TeV is then found to be $\frac{\Delta g_{Hbb}}{g_{Hbb}} = 1.9\%$.

2020 JINST 15 P05001

5.2 Higgs Boson coupling to b quarks at $\sqrt{s}$ = 3 TeV and $\sqrt{s}$ = 10 TeV

The procedure used in section 5.1 is also applied to evaluate the sensitivity to the g_{Hbb} coupling when it is measured in muon collisions at $\sqrt{s}$ = 3.0 TeV and $\sqrt{s}$ = 10 TeV. The approach that is followed is very conservative. The nozzles and the interaction region are not optimized for the higher energies, nor is the detector. The efficiencies obtained with the full simulation at $\sqrt{s}$ = 1.5 TeV are used for the higher center-of-mass energy cases, with the proper scaling to take into account the different kinematic region. At higher $\sqrt{s}$ the tracking and the calorimeter detectors are expected to perform significantly better since the yield of the beam-induced background decreases with $\sqrt{s}$ as demonstrated in ref. [7]. The uncertainty on $\frac{g^2_{HWW}}{\Gamma_H}$ at $\sqrt{s}$ = 3.0 TeV is taken from the CLIC study at the same center-of-mass energy [16]. At $\sqrt{s}$ = 10 TeV this uncertainty is assumed equal to the one at $\sqrt{s}$ = 3.0 TeV. For the moment this is the only estimated number and, following the conservative approach that drives this work, it is used as is. It is reasonable to imagine that, when the full Higgs boson couplings analysis will be carried out at $\sqrt{s}$ = 10 TeV, this uncertainty will improve.

The instantaneous luminosity, $\mathcal{L}$, at different $\sqrt{s}$ are taken from ref. [17]. The integrated luminosity, $\mathcal{L}_{\text{int}}$, is calculated by using the standard four Snowmass years. The acceptance, A, the number of signal events, N, and background, B, are determined with simulation. The uncertainties on σ and g_{Hbb} are calculated and summarized in table 2 along with all relevant inputs. The resulting relative uncertainty on the coupling is 1.0% at $\sqrt{s}$ = 3.0 TeV and 0.91% at $\sqrt{s}$ = 10 TeV. It should be noted that the result at $\sqrt{s}$ = 10 TeV is dominated by the error on $\frac{g^2_{HWW}}{\Gamma_H}$, which is assumed equal to the one used at $\sqrt{s}$ = 3 TeV.

Table 2. Summary of the parameters used as inputs for the determination of the Higgs coupling to b quarks. The data taking time is assumed of $4 \cdot 10^7$ s. The parameter definitions are given in the text.

$\sqrt{s}$ [TeV]	A [%]	ϵ [%]	$\mathcal{L}$ [cm^{-2}s^{-1}]	$\mathcal{L}_{\text{int}}$ [ab^{-1}]	σ [fb]	N	B	$\frac{\Delta\sigma}{\sigma}$ [%]	$\frac{\Delta g_{Hbb}}{g_{Hbb}}$ [%]
1.5	35	15	$1.25 \cdot 10^{34}$	0.5	203	5500	6700	2.0	1.9
3.0	37	15	$4.4 \cdot 10^{34}$	1.3	324	33000	7700	0.60	1.0
10	39	16	$2 \cdot 10^{35}$	8.0	549	270000	4400	0.20	0.91

6 Comparison to CLIC

The direct comparison of the results obtained on $\frac{\Delta g_{Hbb}}{g_{Hbb}}$ at a muon collider with other colliders, as done in ref. [18], is not yet available. In order to evaluate the potential of an experiment at a muon collider, these results are compared to those published by CLIC [16]. CLIC numbers are obtained with a model-independent multi-parameter fit. In addition, the fit is performed in three stages, taking the statistical uncertainties obtainable at the three considered energies successively into account. This means that each new stage includes all measurements of the previous stages and is represented in table 3 with a "+" in the integrated luminosity.

The muon collider results are not complete, since not all the necessary parameters are determined. They are based on assumptions that are very conservative, as discussed in the previous sections. Data samples at the three center-of-mass energies are treated as independent, and not

2020 JINST 15 P05001

taken successively into account. This means that at $\sqrt{s} = 3\,\text{TeV}$ the precision achieved by the experiment at muon collider uses 4 data-taking years while the CLIC number includes also the 4 years at $\sqrt{s} = 350\,\text{GeV}$.

Table 3. Relative precision on Higgs boson coupling to b-quark at muon collider and at CLIC. The difference on how the numbers are obtained by the two experiments is described in the text.

	$\sqrt{s}$ [TeV]	$\mathcal{L}_{\text{int}}$ [ab^{-1}]	$\frac{\Delta g_{Hbb}}{g_{Hbb}}$ [%]
Muon Collider	1.5	0.5	1.9
	3.0	1.3	1.0
	10	8.0	0.91
CLIC	0.35	0.5	3.0
	1.4	+1.5	1.0
	3.0	+2.0	0.9

7 Summary and conclusion

A detailed study of the Higgs boson decay to b-jets at $\sqrt{s} = 1.5\,\text{TeV}$ is presented, based on a full simulation of the physics process and the beam-induced background. The physics performance of the tracking and calorimeter detectors is discussed together with new ideas to mitigate the effect of the beam-induced background. The Higgs boson decay to b-jets is efficiently reconstructed demonstrating that the beam-induced background does not jeopardize physics performance of an experiment at a muon collider. These results demonstrate that high energy muon collisions perform better than electron-positron machines thanks to the almost negligible beamstrahlung and synchrotron radiation. The uncertainty on the Higgs boson coupling to b-quarks is determined under several assumptions and compared to the results obtained by CLIC in similar conditions. CLIC has quoted the best precision on g_{Hbb} [18] and the fact that the muon collider provides similar numbers in a non-optimized configuration shows its potential. A study of the Higgs couplings to fermions and bosons is in progress with high priority given to evaluating the Higgs self-coupling.

Acknowledgments

We owe a huge debt of gratitude to Anna Mazzacane and Vito Di Benedetto (FNAL) who made this study possible by providing us with the MAP's software framework and simulation code. We acknowledge support from Istituto Nazionale di Fisica Nucleare. We thank the VenetoCloud for providing computing resources and Lucio Strizzolo and the IT team of INFN Trieste for their technical support with the local cloud computing. The research leading to these results has received funding from the project LUCC_SID18_01 of the Department of Physics and Astronomy of the University of Padova. US efforts in support of this analysis framework were supported under US Department of Energy Contracts DE-SC0012704 and DE-AC02-07CH11359.

2020 JINST 15 P05001

References

[1] N.V. Mokhov, V.V. Kashikhin, S.I. Striganov, I.S. Tropin and A.V. Zlobin, *The Higgs Factory Muon Collider Superconducting Magnets and Their Protection Against Beam Decay Radiation*, 2018 *JINST* **13** P10024 [arXiv:1806.08883].

[2] G.W. Foster and N.V. Mokhov, *Backgrounds and detector performance at a 2 ×2 TeV $\mu^+\mu^-$ collider*, *AIP Conf. Proc.* **352** (1996) 178.

[3] N.V. Mokhov and S.I. Striganov, *Detector Background at Muon Colliders*, *Phys. Procedia* **37** (2012) 2015 [arXiv:1204.6721].

[4] N.V. Mokhov, S.I. Striganov and I.S. Tropin, *Reducing Backgrounds in the Higgs Factory Muon Collider Detector*, in *Proceedings of the 5th International Particle Accelerator Conference (IPAC 2014)*, Dresden, Germany, 15–20 June 2014, pp. 1081–1083 [arXiv:1409.1939].

[5] *The Muon Accelerator Program*, https://map.fnal.gov/.

[6] N.V. Mokhov and C.C. James, *The MARS code system user's guide version 15(2016)*, Fermilab-FN-1058-APC (2018) [DOI:10.2172/1462233].

[7] N. Bartosik et al., *Preliminary Report on the Study of Beam-Induced Background Effects at a Muon Collider*, arXiv:1905.03725.

[8] V. Di Benedetto, C. Gatto, A. Mazzacane, N.V. Mokhov, S.I. Striganov and N.K. Terentiev, *A Study of Muon Collider Background Rejection Criteria in Silicon Vertex and Tracker Detectors*, 2018 *JINST* **13** P09004 [arXiv:1807.00074].

[9] C. Gatto et al., *The IlcRoot FrameWork*, http://www.dmf.unisalento.it/ danieleb/IlcRoot/.

[10] N. Cartiglia et al., *Tracking in 4 dimensions*, *Nucl. Instrum. Meth.* **A 845** (2017) 47.

[11] W. Riegler and G. Aglieri Rinella, *Time resolution of silicon pixel sensors*, 2017 *JINST* **12** P11017 [arXiv:1706.04883].

[12] C. Gatto, V. Di Benedetto, E. Hahn and A. Mazzacane, *Status of Dual-readout R&D for a Linear Collider in T1015 Collaboration*, in *Proceedings of the International Workshop on Future Linear Colliders (LCWS15)*, Whistler, B.C., Canada, 2–6 November 2015, http://lss.fnal.gov/archive/2015/conf/fermilab-conf-15-689-e.pdf [arXiv:1603.00909].

[13] UA1 collaboration, *Hadronic Jet Production at the CERN Proton - anti-Proton Collider*, *Phys. Lett.* **132B** (1983) 214.

[14] T. Sjöstrand, S. Mrenna and P.Z. Skands, *A Brief Introduction to PYTHIA 8.1*, *Comput. Phys. Commun.* **178** (2008) 852 [arXiv:0710.3820].

[15] LHCb collaboration, *Identification of beauty and charm quark jets at LHCb*, 2015 *JINST* **10** P06013 [arXiv:1504.07670].

[16] H. Abramowicz et al., *Higgs physics at the CLIC electron–positron linear collider*, *Eur. Phys. J.* **C 77** (2017) 475 [arXiv:1608.07538].

[17] J.-P. Delahaye et al., *Enabling Intensity and Energy Frontier Science with a Muon Accelerator Facility in the U.S.: A White Paper Submitted to the 2013 U.S. Community Summer Study of the Division of Particles and Fields of the American Physical Society*, in *Proceedings of the 2013 Community Summer Study on the Future of U.S. Particle Physics: Snowmass on the Mississippi (CSS2013)*, Minneapolis, MN, U.S.A., 29 July–6 August 2013, http://www.slac.stanford.edu/econf/C1307292/docs/submittedArxivFiles/1308.0494.pdf [arXiv:1308.0494].

[18] J. de Blas et al., *Higgs Boson Studies at Future Particle Colliders*, *JHEP* **01** (2020) 139 [arXiv:1905.03764].

2020 JINST 15 P05001